Modeling and Comparative Performance Analysis of Perovskite Solar Cells with Planar or Nanorod SnO_2 Electron-Transport Layers

Assylan Akhanuly,[1,†] Iliyas T. Dossyaev,[1,2,†] Erik O. Shalenov,[1,3,4] Constantinos Valagiannopoulos,[1] Karlygash N. Dzhumagulova,[1,3,4] Annie Ng,[5] and Askhat N. Jumabekov[1,*]

[1] *Department of Physics, School of Sciences and Humanities, Nazarbayev University, Astana 010000, Kazakhstan*
[2] *Department of Mathematics, School of Sciences and Humanities, Nazarbayev University, Astana 010000, Kazakhstan*
[3] *Department of General Physics, Satbayev University, Almaty 050013, Kazakhstan*
[4] *Institute of Experimental and Theoretical Physics, al-Farabi Kazakh National University, Almaty 050040, Kazakhstan*
[5] *Department of Electrical and Computer Engineering, School of Engineering and Digital Sciences, Nazarbayev University, Astana 010000, Kazakhstan*

(Received 30 October 2022; revised 21 February 2023; accepted 13 March 2023; published 11 May 2023)

Application of various electron-transport layers (ETLs) with desired morphology and dimensions is a key factor to be considered for the structural designs of perovskite solar cells (PSCs) in order to obtain enhanced optical and electrical properties. The metal-oxide ETLs composed of one-dimensional nanorod arrays are one of the most frequently used nanostructures for electron transporting in PSCs. In this work, computer-simulation methods are employed to investigate the optoelectrical properties of PSCs with planar and nanorod-based SnO_2 ETLs. A two-dimensional optical model is used to determine the optical responses of devices and the standard drift-diffusion model is utilized to simulate their behavior and performance. The aspect ratio and the density of SnO_2 nanorods are varied to examine their effect on the optical and the electrical properties of resulting devices and the findings are contrasted with those of planar devices. It is found that under optimum conditions, PSCs with thin planar SnO_2 ETLs, which are referred to as reference planar devices, outperform PSCs with nanorod-based SnO_2 ETLs even if the light-harvesting properties of the latter are improved with the implementation of structured ETLs. The underlying reasons for this phenomenon are analyzed and rationalized through a detailed analysis and comparison of electric field, current density, and carrier recombination distributions in PSCs. The findings of this work can be used as a theoretical guide for designing and fabrication of high-performance planar and structured PSCs using SnO_2 ETLs.

DOI: 10.1103/PhysRevApplied.19.054039

I. INTRODUCTION

Halide perovskite materials belong to a promising class of semiconductors for next-generation photovoltaic (PV) devices, which have generated enormous interests in the research community since 2009 [1–3]. These materials possess excellent optoelectronic properties, such as tunable band gap, high light absorption in the visible and UV spectral ranges, long charge-carrier diffusion length, and low nonradiative charge-carrier recombination rates [4,5]. Additionally, perovskites are cheap, abundant, and solution-processable materials that do not require high-temperature processing [1–3]. Solar cells based on perovskites have reached power-conversion-efficiency (PCE) values as high as 25.7% for single-junction devices and 32.5% for silicon and perovskite tandem devices [6]. This is a remarkable improvement in the performance of perovskite solar cells (PSCs) considering that a PCE value for solar-cell devices employing a perovskite material as a photoabsorber layer was only 3.9% in 2009 [7].

A number of studies have been reported in the literature in recent years, in which the effects of the electron-transport-layer (ETL) structures on the performance of PSCs are investigated [8–30]. The comparative studies performed on ETLs with various structures indicate that vertically aligned nanorods [one dimensional (1D)] and, in some cases, vertically aligned nanosheets [two dimensional (2D)] of metal oxides, such as TiO_2, ZnO, or SnO_2 can perform better in PSCs than their three-dimensional (3D) porous or planar alternatives [10–14]. It has been reported that ETLs with 1D structures enable

*Corresponding author. askhat.jumabekov@nu.edu.kz
†These authors contributed equally.

deposition of uniform perovskite layers with less pinholes, high crystallinity, and large grain sizes [17–20]. A better performance of PSCs with 1D-structured ETLs is attributed to reduced grain boundaries and reduced trap states, while the vertically aligned nanorods of ETLs afford a better charge collection [25,26]. Additionally, it is found that the morphology of 1D-structured ETLs improves the light-harvesting ability of devices due to light-trapping effects in nanorods [20,21]. Also, PSCs with 1D ETLs are reported to have a better stability than the ones with porous ETLs [29].

Despite all the advantages provided by 1D-structured metal-oxide ETLs, surveying the literature for the best-performing PSCs indicate that devices with outstanding PCEs are usually obtained using ETLs with porous or planar structures [31–37]. As a result, the effect of 1D-structured metal-oxide ETLs in obtaining high-performance PSCs requires more detailed analysis and investigation. Therefore, the aim of this work is to assess whether the use of 1D-structured metal-oxide ETLs can produce PSCs with improved performance compared to their planar alternatives. In this study, PSCs with nanorod-based SnO_2 ETLs are investigated using computer-simulation methods and their performance is contrasted with the performance of PSCs employing planar SnO_2 ETLs. The numerical simulations are conducted for different aspect ratios and density of SnO_2 nanorods, considering the optimum electronic parameters of the materials used for the device functional layers [ETL, hole-transport layer (HTL), and perovskite photoabsorber layer]. The discrepancies in the performance of compared devices are investigated and the underlying reasons are revealed based on the computer-simulation results.

II. EXPERIMENTAL DETAILS

A. Theoretical approach and computational details

Computer simulations of the optoelectric properties of devices are carried out by applying the standard drift-diffusion model for semiconductors and multidimensional optical simulation approach reported by Li *et al.* [38–44]. The optical simulation approach by Li *et al.* is a powerful method, which allows estimation of carrier generation rates in devices more accurately and is based on calculation of spectrally dependent power flow (Poynting vector) across the volume of devices in all three dimensions [41]. The method takes into account absorption and transmission of incident electromagnetic waves (light) in every device functional layer and accounts for light reflection at each interface in-between. Hence, when carrier generation rates in devices is calculated using this method, any optical process that might take place in devices is accounted. The detailed description of the equations, the standard drift-diffusion model (Poisson equation, equations for electron and hole currents, and continuity equation), and the multidimensional optical simulation approach for calculating the spatial charge-carrier generation rates in devices are provided below.

1. Poisson equation

$$\nabla \cdot (-\varepsilon_0 \varepsilon_r \nabla V) = \rho\,(x,y,z)\,, \tag{1}$$

where $\rho(x,y,z) = q(p(x,y,z) - n(x,y,z) + N_d^+(x,y,z) - N_a^-(x,y,z))$. Here, ε_0 is the vacuum permittivity, ε_r is the dielectric constant of the perovskite layer, q is the elementary charge. $p(x,y,z)$ and $n(x,y,z)$ are the local concentrations of holes and electrons, respectively, while $N_d^+(x,y,z)$ and $N_a^-(x,y,z)$ are the local donor and acceptor concentrations, respectively. For calculation of $p(x,y,z)$ and $n(x,y,z)$, the following relations are used:

$$n = \frac{1}{2}\left(\left(N_d^+ - N_a^-\right) + \sqrt{\left(N_d^+ - N_a^-\right)^2 + 4n_i^2}\right), \tag{2}$$

$$p = -\frac{1}{2}\left(\left(N_d^+ - N_a^-\right) + \sqrt{\left(N_d^+ - N_a^-\right)^2 + 4n_i^2}\right), \tag{3}$$

where $n_i = \sqrt{N_{c0}N_{v0}}\exp\left(-E_g/2k_BT\right)$. Here, n_i is the intrinsic concentration of charge carriers, N_{c0} and N_{v0} are the effective density of states in the conduction and valence bands, respectively, E_g is the band gap, k_B is Boltzmann's constant, and T is the absolute temperature.

2. Electron and hole currents

$$\nabla \cdot J_n = 0, \tag{4}$$

$$\nabla \cdot J_p = 0, \tag{5}$$

$$J_n = qn\mu_n E_c + \mu_n k_B T \nabla n, \tag{6}$$

$$J_p = qp\mu_p E_v + \mu_p k_B T \nabla p, \tag{7}$$

$$E_c = -\nabla\,(V + \chi_0)\,, \tag{8}$$

$$E_v = -\nabla\left(V + \chi_0 + E_g\right), \tag{9}$$

$$L_{d,n} = \sqrt{D_n \tau_n}, \tag{10}$$

$$L_{d,p} = \sqrt{D_p \tau_p}, \tag{11}$$

$$D_n = \frac{\mu_n k_B T}{q}, \tag{12}$$

$$D_p = \frac{\mu_p k_B T}{q}, \tag{13}$$

where J_n is electron current density, J_p is hole current density, μ_n is mobility of electrons, μ_p is mobility of holes, E_c is conduction-band energy, E_v is valence-band energy, χ_0

is electron affinity, $L_{d,n}$ is diffusion length of electrons, $L_{d,p}$ is diffusion length of holes, τ_n is electron lifetime, and τ_p is hole lifetime.

3. Continuity equations

$$\frac{\partial n}{\partial t} = G_n - R_n + \frac{1}{q}\nabla \cdot J_n, \tag{14}$$

$$\frac{\partial p}{\partial t} = G_p - R_p + \frac{1}{q}\nabla \cdot J_p, \tag{15}$$

where G_n and G_p are unit-volume generation rates for electrons and holes, R_n and R_p are recombination rates for electrons and holes (Shockley-Read-Hall). The Shockley-Read-Hall recombination rate [45] is

$$R_n = \frac{np - n_i^2}{\tau_p(n + n_i) + \tau_n(p + p_i)} = R_p, \tag{16}$$

$$\nabla \cdot J_n = qR_n,\ \nabla \cdot J_p = qR_p. \tag{17}$$

4. Multidimensional charge-carrier generation rate

The optical part of the simulations is carried out by calculating the spatial generation rate of the electron-hole pair in the perovskite layer:

$$G(x,y,z) = \int_{\lambda_1}^{\lambda_2} \alpha(\lambda)\,\varphi(\lambda)\,P_s(x,y,z,\lambda)d\lambda, \tag{18}$$

where λ_1 and λ_2 are the minimum and maximum wavelength of incident light, respectively. In addition, $\alpha(\lambda)$ is the perovskite-layer absorption coefficient, $\varphi(\lambda)$ is photon flux, and $P_s(x,y,z,\lambda)$ is power flow (Poynting vector), defined by the following expressions:

$$\alpha(\lambda) = \frac{4\pi\kappa(\lambda)}{\lambda}, \tag{19}$$

$$\varphi(\lambda) = \frac{\lambda}{hc}F(\lambda), \tag{20}$$

$$P_s(x,y,z,\lambda) = \sqrt{|P_{0x}(x,y,z,\lambda)|^2 + |P_{0y}(x,y,z,\lambda)|^2 + |P_{0z}(x,y,z,\lambda)|^2}, \tag{21}$$

where λ is wavelength of incident electromagnetic wave, $\kappa(\lambda)$ is the imaginary part of the refractive index, $F(\lambda)$ is the spectral irradiance (AM1.5G spectrum). $P_{0x}(x,y,z,\lambda)$, $P_{0y}(x,y,z,\lambda)$, $P_{0z}(x,y,z,\lambda)$ are x, y, and z components of power flow, respectively, and calculated using the following relations:

$$P_{0x}(x,y,z,\lambda) = \frac{1}{2}\mathrm{Re}(E_yH_z^* - E_zH_y^*), \tag{22}$$

$$P_{0y}(x,y,z,\lambda) = \frac{1}{2}\mathrm{Re}(E_zH_x^* - E_xH_z^*), \tag{23}$$

$$P_{0z}(x,y,z,\lambda) = \frac{1}{2}\mathrm{Re}(E_xH_y^* - E_yH_x^*), \tag{24}$$

where E and H are the electric and magnetic fields, respectively, which depend on the frequency of the incident light on the surface of devices. The symbols "Re" and "*" indicate the real part and complex conjugate of complex numbers, accordingly. Dispersive permittivity ε of materials used in devices is obtained by using the following expression:

$$\varepsilon = (n - ik)^2, \tag{25}$$

where n is refractive index and k is the extinction coefficient of material. The wavelength dependences of n, k, and real part of ε of the employed materials as the device functional layers are presented in Fig. S1 within the Supplemental Material [46–50].

B. Deceive structures for planar and structured PSCs

The general device structures of PSCs with planar and structured ETLs investigated in this work are illustrated in Fig. 1. Here, soda-lime glass, fluorine-doped tin oxide (FTO), SnO_2, methylammonium lead iodide ($MAPbI_3$), 2,2′,7,7′-tetrakis(N,N-di-p-methoxyphenylamino)-9,9′-spirobifluorene (Spiro-OMeTAD), and gold are used as substrate, transparent conductive oxide (TCO) layer, ETL, perovskite layer, HTL, and top metallic contacts, respectively. The height (h) of SnO_2 nanorods in devices varies from 0 to 250 nm, whereas the width (w) of SnO_2 nanorods varies from 0 to 80 nm. The center-to-center distance between adjacent SnO_2 nanorods is set equal to 80 nm. The base for SnO_2 nanorods in devices is composed of a 15-nm SnO_2 compact layer. Devices, in which $h = 0$ nm and $0 \le w \le 80$ nm or $0 \le h \le 250$ nm and $w = 0$ nm, are referred to as "reference planar devices" and the corresponding ETLs are called "reference planar ETLs." Here, the SnO_2 ETL is simply the base SnO_2 layer with a thickness of 15 nm. Devices, in which $0 < h \le 250$ nm and $0 < w < 80$ nm, are referred to as "structured devices"

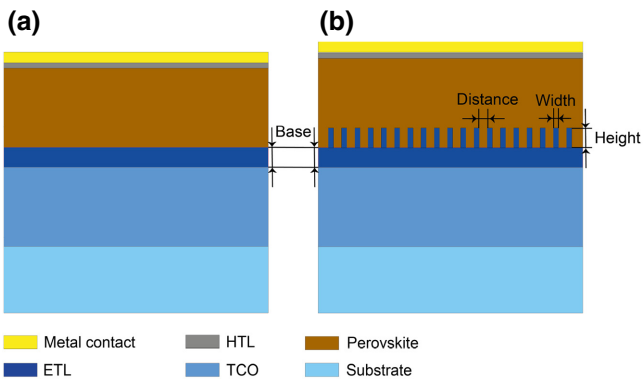

FIG. 1. Schematic representation of (a) planar and (b) structured PSCs.

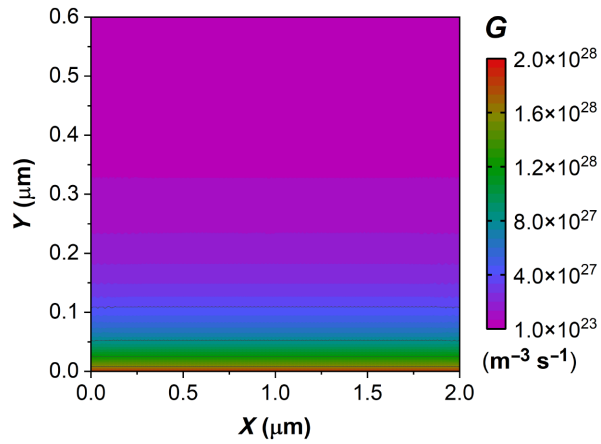

FIG. 2. Perovskite-layer 2D spatial charge-generation profile map for PSC with planar ETL.

and the corresponding ETLs are called "structured ETLs." It should be noted that when $w = 80$ nm and $0 < h \leq 250$ nm, the walls of the SnO_2 nanorods in the structured ETLs merge with each other. As a result of this, the corresponding devices also present PSCs with planar but thick ETLs (thicker than the 15-nm base SnO_2 layer). Therefore, these devices are referred to as "thick planar devices" and the corresponding ETLs are called "thick planar ETLs."

C. Geometrical and physical parameters

Regardless of the variations in the geometric dimensions and density of SnO_2 nanorods, the perovskite layer volume (PSK_V) to the device active area (S_D) ratio, which is denoted as $\Omega = PSK_V/S_D$, is kept equal to 600 nm^3 nm^{-2} in all devices in order to ensure fair comparisons between devices with planar and structured ETLs. The details of geometrical dimensions of devices are summarized in Table S1 within the Supplemental Material [46], whereas the physical parameters of materials used for the device functional layers are summarized in Table I.

III. RESULTS AND DISCUSSION

A. Charge-carrier generation in planar and structured PSCs

To obtain a careful characterization and comparison of device properties, the exact optical responses of PSCs with planar and structured ETLs are calculated using Eqs. (18)–(25). Figure 2 shows the perovskite layer 2D spatial charge-carrier generation-rate profile map calculated for reference planar PSCs under 1-Sun condition (100 mW cm^{-2} at AM1.5G solar irradiance). As expected, carrier generation in the perovskite layer is the highest near the ETL side ($Y = 0$ μm) and decays exponentially closer to the HTL side ($Y = 0.6$ μm). This indicates that regular Lambert-Beer optical absorption model can also be used to calculate charge-carrier generation rate in PSCs with planar ETLs [39].

Figure 3 shows the perovskite-layer 2D spatial charge-carrier generation-rate profile maps calculated for PSCs under 1-Sun condition, for various h and w, whose complete data is presented in Fig. S2 (see Supplemental

TABLE I. Parameters of materials for electrical stimulation.

Parameters and units	Spiro-OMeTAD (HTL)	Perovskite	SnO_2 (ETL)
Dielectric constant	3 [51]	30 [40]	9 [40]
Band gap (V)	3.2 [51]	1.55 [40]	3.7 [40]
Electron affinity (V)	2.1 [51]	3.9 [40]	4.23 [40]
Electron mobility (cm^2 V^{-1} s^{-1})	2×10^{-4} [51]	10	20 [40]
Hole mobility (cm^2 V^{-1} s^{-1})	2×10^{-4} [51]	10	10 [40]
Electron lifetime (s)	...	10^{-6}	...
Hole lifetime (s)	...	10^{-6}	...
Acceptor concentration (cm^{-3})	10^{17} [51]	...	...
Donor concentration (cm^{-3})	...	10^{12}	2×10^{16}
Effective conduction-band density (cm^{-3})	2.5×10^{18} [51]	4.42×10^{17} [40]	2.2×10^{18} [40]
Effective valence-band density (cm^{-3})	1.8×10^{19} [51]	8.72×10^{18} [40]	2.2×10^{19} [40]
Surface recombination velocity (cm s^{-1})	...	1	...

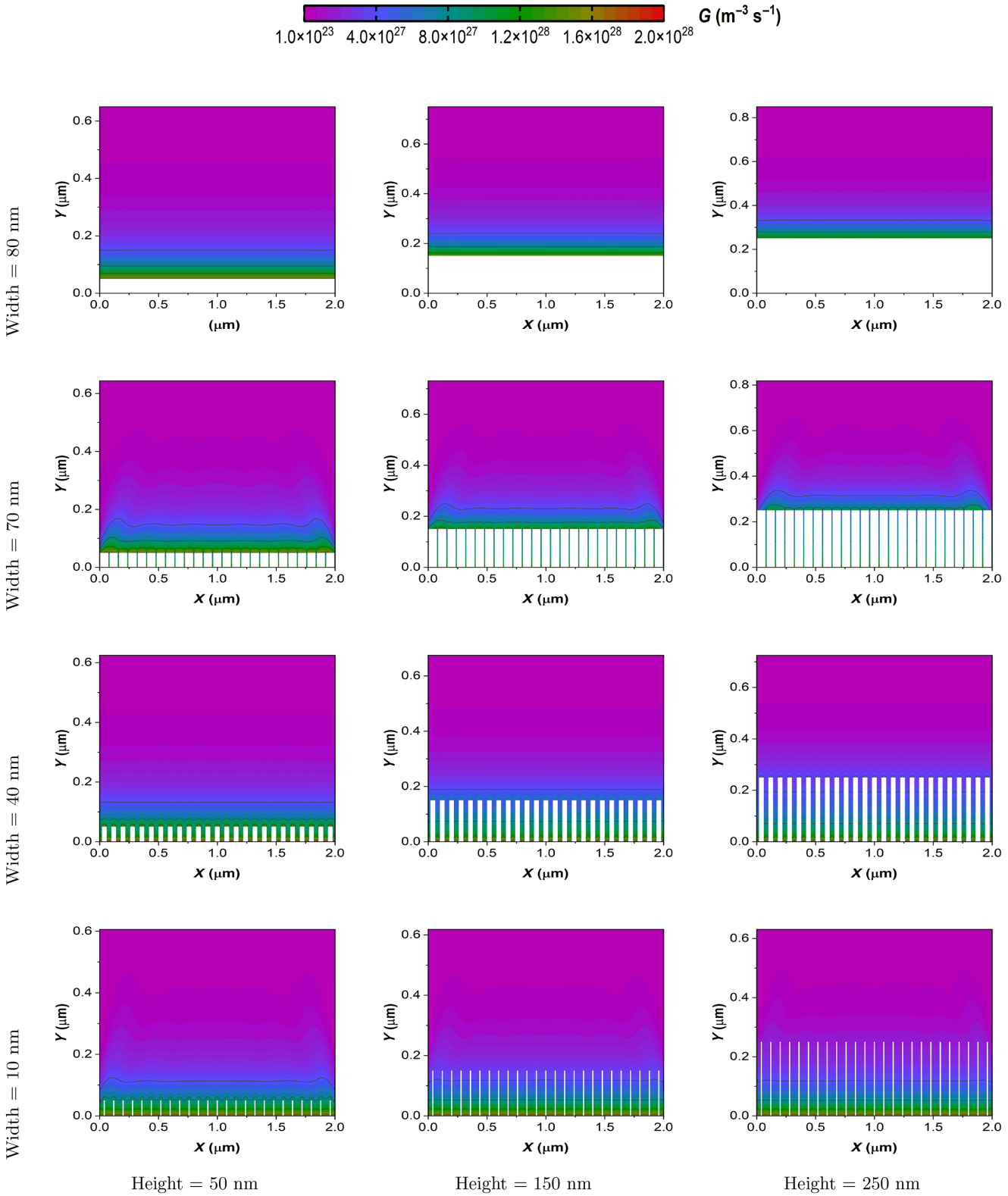

FIG. 3. Perovskite layer 2D spatial charge-generation profile maps for PSCs with structured ETLs.

Material [46]). The graphs at $w = 10, 40$, and 70 nm in Fig. 3 show the perovskite layer 2D spatial charge-carrier generation-rate profile maps in structured devices, whereas the graphs at $w = 80$ nm show the perovskite-layer 2D spatial charge-carrier generation-rate profile maps in thick planar devices. Similar to Fig. 2, carrier generation in the perovskite layer is the highest near the ETL side and subsides close to the HTL side. Unlike in devices with planar ETLs, charge-carrier generation-rate profile maps in structured devices have certain irregularities as shown in Fig. 3. This is due to ETL SnO_2 nanorods that influence the propagation and absorption of incident light in the perovskite layer. Hence, these results indicate that the applied multidimensional optical absorption is useful in obtaining more accurate values of charge-carrier generation rate in the bulk of the perovskite layer in devices with structured ETLs [39–41].

Since Ω is set to be constant in all devices, the averaged values of charge-carrier generation rates (G_{avg}) in devices can be compared to assess the effect of ETLs' structure on the light harvesting and the charge-carrier generation abilities. To do this, the G_{avg} value in each 2D spatial charge-carrier generation-rate profile map (see Figs. 2 and S2 within the Supplemental Material [46]) is calculated and plot against h and w, as shown in Fig. 4.

Figure 4 indicates that the G_{avg} values in planar devices, in general, are smaller than in structured devices. The lowest G_{avg} value (1.83×10^{27} m^{-3} s^{-1}) is obtained for devices with the thickest planar ETL ($w = 80$ nm and $h = 250$ nm), whereas a slightly higher G_{avg} value (2.62×10^{27} m^{-3} s^{-1}) is for reference planar devices. In addition, Fig. 4 indicates that there are two regions with high G_{avg} values in structured devices. The peaks for high G_{avg} values in both regions appear at the same height ($h = 50$ nm) but at different width (region 1, $w = 10$ nm; region 2, $w =$ 70 nm) of nanorods. The peak G_{avg} values in the region 1 and 2 are 5×10^{27} and 3.92×10^{27} m^{-3} s^{-1}, respectively. With the increase of ETL SnO_2 nanorod heights, the G_{avg} values in region 1 and 2 gradually dissipate as depicted in Fig. 4. The emergence of these two parametric regions with high G_{avg} suggests that the charge-carrier generation rate in structured devices can indeed be improved by employing 1D-structured ETLs. This can be attributed to light trapping in devices due to ETL SnO_2 nanorods [20,21].

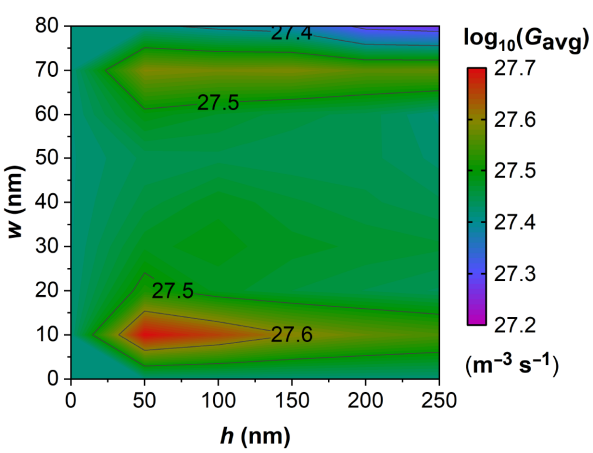

FIG. 4. Dependence of G_{avg} (average charge-carrier generation rate) in the perovskite layer of PSCs on w (width) and h (height) of ETL SnO_2 nanorods.

B. Performance of planar and structured PSCs

Figure 5 depicts how the photovoltaic parameters [current density under short-circuit condition (J_{SC}), open-circuit voltage (V_{OC}), fill factor (FF), and power conversion efficiency (PCE)] of devices under 1-Sun condition depend on h and w values of ETL SnO_2 nanorods. The results indicate that the highest J_{SC} value (22.8 mA cm^{-2}) is obtained in reference planar PSCs; however, note that an increase in h and w values reduces J_{SC} as shown in Fig. 5(a). On the other hand, the smallest J_{SC} value (17.5 mA cm^{-2}) is obtained in thickest planar devices, while the changes in the dimensions of ETL SnO_2 nanorods does not seem to have a considerable effect on V_{OC} and FF [see Figs. 5(b) and 5(c)]. This suggests that the main parameter that strongly influences the performance of devices is J_{SC}. Hence, the highest PCE (23.2%) is obtained in reference planar PSCs, whereas structured devices yield smaller PCE values. The smallest PCE (17.7%) is obtained for thickest planar devices.

A comparative analysis of the results shown in Figs. 4 and 5 indicates that higher charge-carrier generation rates in the perovskite layer (e.g., in structured devices) do not necessarily guarantee higher J_{SC} values and better performances in devices. For instance, according to Fig. 4, the highest G_{avg} value is obtained when h and w values of ETL SnO_2 nanorods are equal to 50 and 10 nm, correspondingly. However, a comparison of the calculated current-density versus voltage (J-V) curves (see Fig. 6) for structured devices with $h = 50$ nm and $w = 10$ nm and reference planar devices show that the J_{SC} of the former is, in fact, slightly lower than the one of reference planar devices. Since the V_{OC} and FF values in both devices are almost the same, the PCE value of reference planar devices is slightly higher than the PCE value of structured devices (Table II). This peculiar finding suggests that for the same device and material parameters, the PCE values of structured devices do not exceed the respective values of reference planar ones.

It should be noted that 50 and 10 nm for the height and width of ETL SnO_2 nanorods is rather small. A typical height and width of ETL SnO_2 nanorods employed in experiments are around 150 and 40 nm, respectively [5]. Hence, it is more appropriate to consider ETL SnO_2

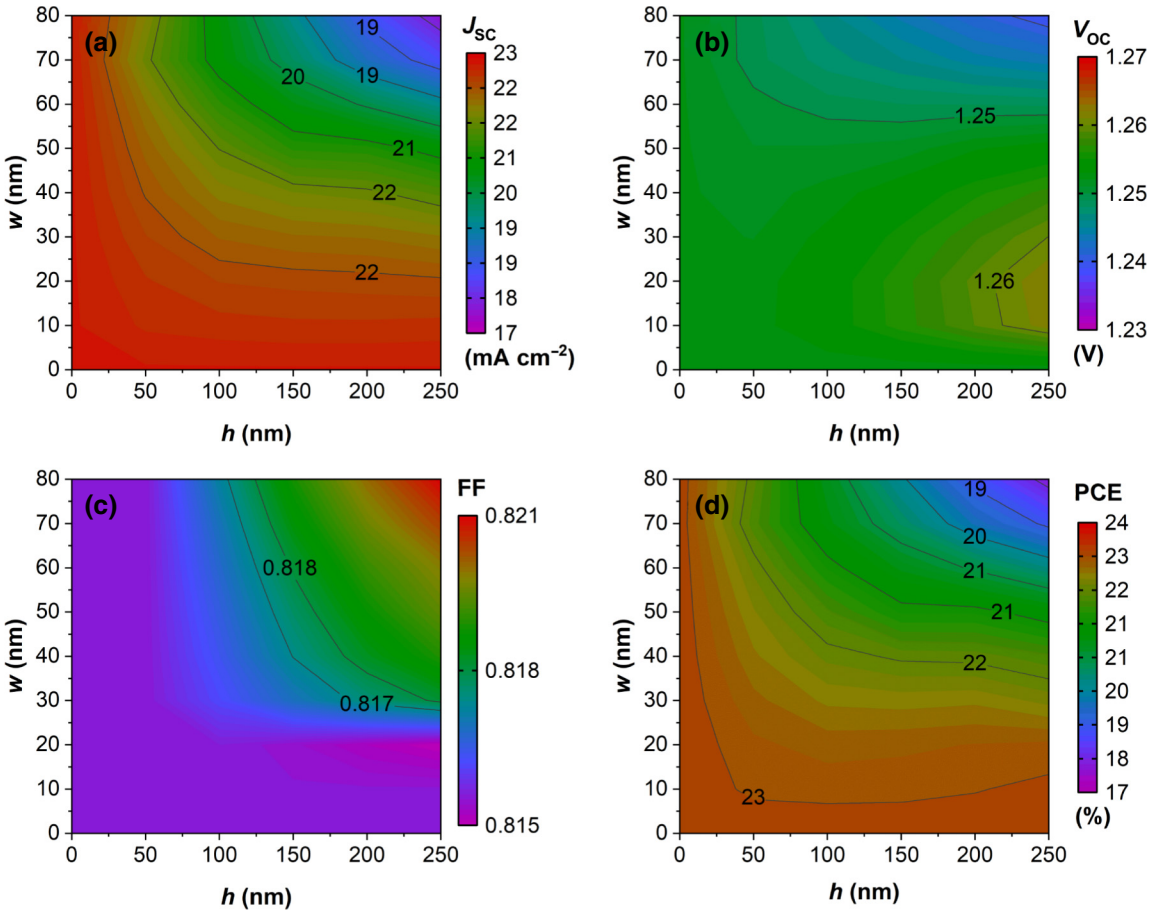

FIG. 5. Dependences of (a) J_{SC}, (b) V_{OC}, (c) FF, and (d) PCE on the w (width) and h (height) of ETL SnO_2 nanorods in PSCs.

nanorods with dimensions that are similar to the experimentally reported values (e.g., h and w around 150 and 40 nm). The calculated J-V curve of structured devices under 1-Sun condition and with $h = 150$ nm and $w = 40$ nm for the dimensions of ETL SnO_2 nanorods is also shown in Fig. 6 and the photovoltaic parameters extracted from the J-V curve are presented in Table II. Figure 6 shows that the J_{SC} value of structured devices with $h = 150$ nm and $w = 40$ nm is around 21. mA cm^{-2}. However, this is smaller than the J_{SC} value of structured devices with the highest G_{avg} (region 1: $h = 50$ nm and $w = 10$ nm) by 0.8 mA cm^{-2} and smaller than the J_{SC} value of reference planar devices by 1 mA cm^{-2}. It should be noted that the G_{avg} value at $h = 150$ nm and $w = 40$ nm (2.9×10^{27} m^{-3} s^{-1}) is lower than the highest G_{avg} value at $h = 50$ nm and $w = 10$ nm (region 1) by approximately 42%, however, it is still larger than the one for reference planar devices by approximately 10%. Nevertheless, the PCE of the structured device with $h = 150$ nm and $w = 40$ nm is still lower than the PCE of reference planar devices by around 4%.

In real devices, ETL SnO_2 nanorods in structured devices are not perfectly alighted and can be tilted to certain angles with respect to a vertical line normal to the substrate surface. Hence, it is also worthwhile to know if a slight tilting of ETL SnO_2 nanorods to the left or/and to the right has an effect on the performance of structured devices. Therefore, structured devices with slightly

TABLE II. Photovoltaic parameters of reference planar and structured PSCs.

Device type	J_{SC} (mA cm^{-2})	V_{OC} (V)	FF	PCE (%)
Reference planar	22.8	1.25	0.82	23.4
$h = 50$ nm, $w = 10$ nm	22.6	1.25	0.82	23.2
$h = 150$ nm, $w = 40$ nm	21.8	1.26	0.82	22.5
$h = 150$ nm, $w = 40$ nm (tilted)	21.8	1.26	0.82	22.5

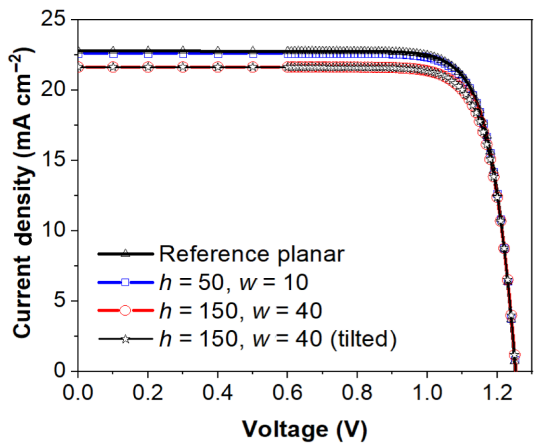

FIG. 6. J-V curves for reference planar and structured PSCs. The heights of ETL SnO_2 nanorods in structured devices are 50 and 150 nm and the corresponding widths are 10 and 40 nm, respectively.

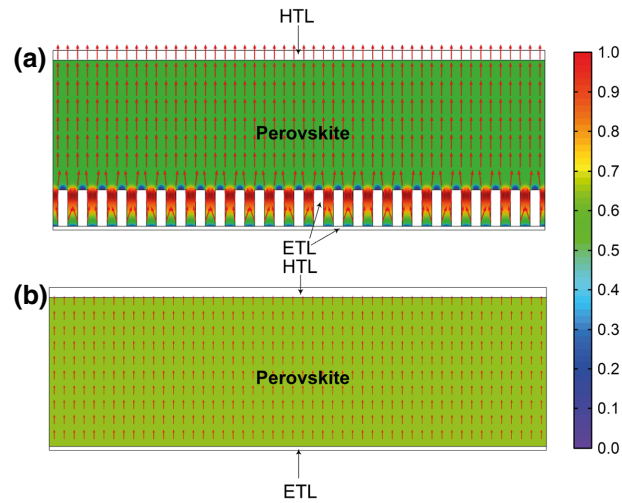

FIG. 7. Normalized electric field distribution in the perovskite layer of (a) structured ($h = 150$ nm and $w = 40$ nm) and (b) reference planar PSCs under short-circuit condition. Arrows represent the directions of the electric field.

and randomly tilted ETL SnO_2 nanorods, in which the dimensions of the ETL SnO_2 nanorods are kept the same as above ($h = 150$ nm and $w = 40$ nm), is also analyzed. For this, a perovskite-layer charge-carrier generation-rate profile map of a structured devices with tilted ETL SnO_2 nanorods is estimated for 1-Sun condition (see Fig. S3 within the Supplemental Material [46]) and used to calculate the device J-V curve. Comparison of the J-V curves (see Fig. 6) and the photovoltaic parameters (see Table II) of the devices with perfectly aligned and tilted ETL SnO_2 nanorods indicate that moderate tilting of ETL SnO_2 nanorods do not have any noticeable effect on the performance of structured devices. This implies that employing perfectly aligned ETL SnO_2 nanorods in this work can be regarded as a representative condition for further investigation of varying the lengths and widths of SnO_2 nanorods in numerical modeling of structured PSCs and analyze their device properties.

C. Electric field and current-density distributions in reference planar and structured PSCs

In order to identify the underlying reason for the discrepancy between the J_{SC} values in reference planar and structured ($h = 150$ nm and $w = 40$ nm) devices, it is necessary to analyze the factors that contribute to charge-current flow in the perovskite layer in these cases. In the calculations, the charge-carrier diffusion coefficient in the perovskite layer of reference planar and structured devices is the same. Hence, the diffusion components of the electric current in both types of devices can be considered the same. The drift component of the electric current depends on the electric field distribution within devices, in which the latter is strongly influenced by the structure. Since the interfaces between the perovskite layer and SnO_2 ETLs are different for reference planar and structured device configurations, it is necessary to analyze closely the spatial electric field distributions within these devices under short-circuit condition. This can help to rule out the origin of the difference in the J_{SC} values between reference planar and structured devices.

The spatial electric field distribution can be obtained by solving the Poisson equation [see Eq. (1)] under short-circuit condition. Figure 7 shows the calculated cross-section 2D electric field distribution maps within the perovskite layers of structured and reference planar device configurations. For a better comparison, the electric field values in both cases are normalized to the maximum value of the field in the perovskite layer of structured devices. Figure 7(a) shows that the electric field in structured devices is homogeneous in the region between HTL and close to the tips of ETL SnO_2 nanorods. Around ETL SnO_2 nanorods, however, the electric field is rather nonhomogeneous; in particular, in between nanorods. The electric field is initially strong but then it quickly dissipates close to the base of nanorods. Above the tips of ETL SnO_2 nanorods, the electric field is rather weak, meaning that charge-carrier separation in structured devices is most effective around the upper parts of nanorods. However, the carrier separation in the region between HTL and close to the tips of ETL SnO_2 nanorods as well as near their base, is rather weak. Moreover, the weakest carrier separation occurs in the region exactly above ETL SnO_2 nanorods. In reference planar devices [Fig. 7(b)], on the other hand, the electric field is homogeneous across the entire perovskite medium, indicating a homogeneous carrier separation throughout the perovskite layer.

It should be noted that in structured devices, the volume fraction of the perovskite layer between nanorods is small. Therefore, when keeping the same Ω values in both devices, the thickness of the perovskite layer from the tips of ETL SnO_2 nanorods to HTL in structured devices (660 nm) is comparable to the thickness of the perovskite layer in reference planar devices (600 nm). At the same time, the electric field strength between the tips of ETL SnO_2 nanorods to HTL in structured devices is slightly weaker than in reference planar devices. This suggests that despite the effective charge separation around ETL SnO_2 nanorods (except for the tips), the overall charge separation in structured devices is slightly inferior to the one in reference planar devices.

Figure 8 shows the cross-section 2D spatial distribution maps of the electron and the hole current densities (J_n and J_p) in structured and reference planar devices. Figure 8(a) depicts that the distribution of J_n in structured devices is highly inhomogeneous as compared to reference planar devices. In structured devices, J_n is highest within ETL SnO_2 nanorods and lowest within HTL. Within the perovskite layer, J_n gradually increases from HTL to the tips of ETL SnO_2 nanorods and then decreases between nanorods. This is consistent with the electric field distribution profile in structured devices [see Fig. 7(a)], which shows that most of the electric field inhomogeneity appears around ETL SnO_2 nanorods. In reference planar devices, J_n gradually increases from HTL to ETL [see Fig. 8(b)]. However, the total J_n in structured devices (6.4 mA cm^{-2}) is higher than the one in reference planar devices (4.5 mA cm^{-2}) by around 1.9 mA cm^{-2} (see Table III).

As for J_p, reference planar devices have its minimum J_p value in ETL, which then quickly increases to its rather homogeneous value (22.04 mA cm^{-2}) across the perovskite layer and HTL [see Fig. 8(d)]. This indicates that J_p in reference planar devices is strong and homogeneous. A similar trend is observed in J_p of structured devices except for some inhomogeneities around the tip of ETL SnO_2 nanorods [see Fig. 8(c)]. However, the J_p values (approximately 20.66 mA cm^{-2}) in the region between the tips of ETL SnO_2 nanorods and HTL in structured devices are slightly lower than the one in reference planar devices. The total J_p in reference planar devices (18.3 mA cm^{-2}) is higher than the one in structured one (15.4 mA cm^{-2}) by 2.9 mA cm^{-2} (see Table III).

TABLE III. J_n, J_p, and J_{tot} values in structured ($h = 150$ nm and $w = 40$ nm) and reference planar PSCs.

Device type	J_n (mA cm^{-2})	J_p (mA cm^{-2})	J_{tot} (mA cm^{-2})
Structured	6.4	15.4	21.8
Reference planar	4.5	18.3	22.8

The sum of J_n and J_p gives the total current (J_{tot}) in devices. Adding the J_n and the J_p values yields 21.8 and 22.8 mA cm^{-2} for the J_{tot} in structured and reference planar devices, correspondingly (see Table III). This is consistent with the J_{SC} values obtained from the simulated J-V curves for these devices (see Fig. 6 and Table II). A higher J_{tot} value in reference planar devices is due to its strong J_p, which is sufficient to compensate for its small J_n and to produce the J_{tot} value that is higher than the J_{tot} of structured devices.

D. Performance of structured PSCs versus internanorod distance in structured SnO_2 ETLs

The influence of the internanorod distance (the distance between the walls of neighboring nanorods) in structured SnO_2 ETLs (see Fig. 1) on the performance of structured PSCs is also a relevant aspect. This provides some insights on how the photovoltaic parameters of structured PSCs depend on the density of ETL SnO_2 nanorods. Therefore, the internanorod distance in ETL SnO_2 nanorods is varied from approximately 1.5 nm to 1600 nm and the performances of corresponding devices are estimated. Here, the dimensions of ETL SnO_2 nanorods are kept the same as above, i.e., $h = 150$ nm and $w = 40$ nm. The calculated

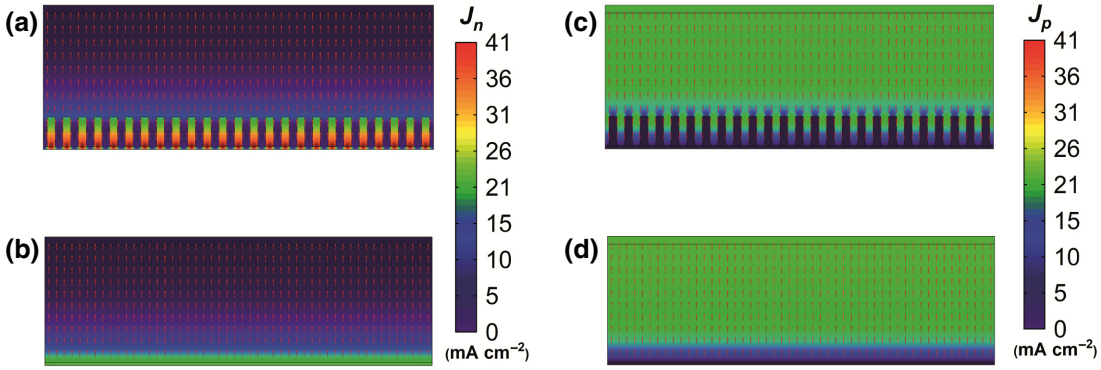

FIG. 8. Cross-section 2D spatial distribution maps of electron (J_n) and hole (J_p) current densities in PSCs. (a),(c) J_n and J_p in structured ($h = 150$ nm and $w = 40$ nm) devices, whereas (b),(d) show J_n and J_p in reference planar devices.

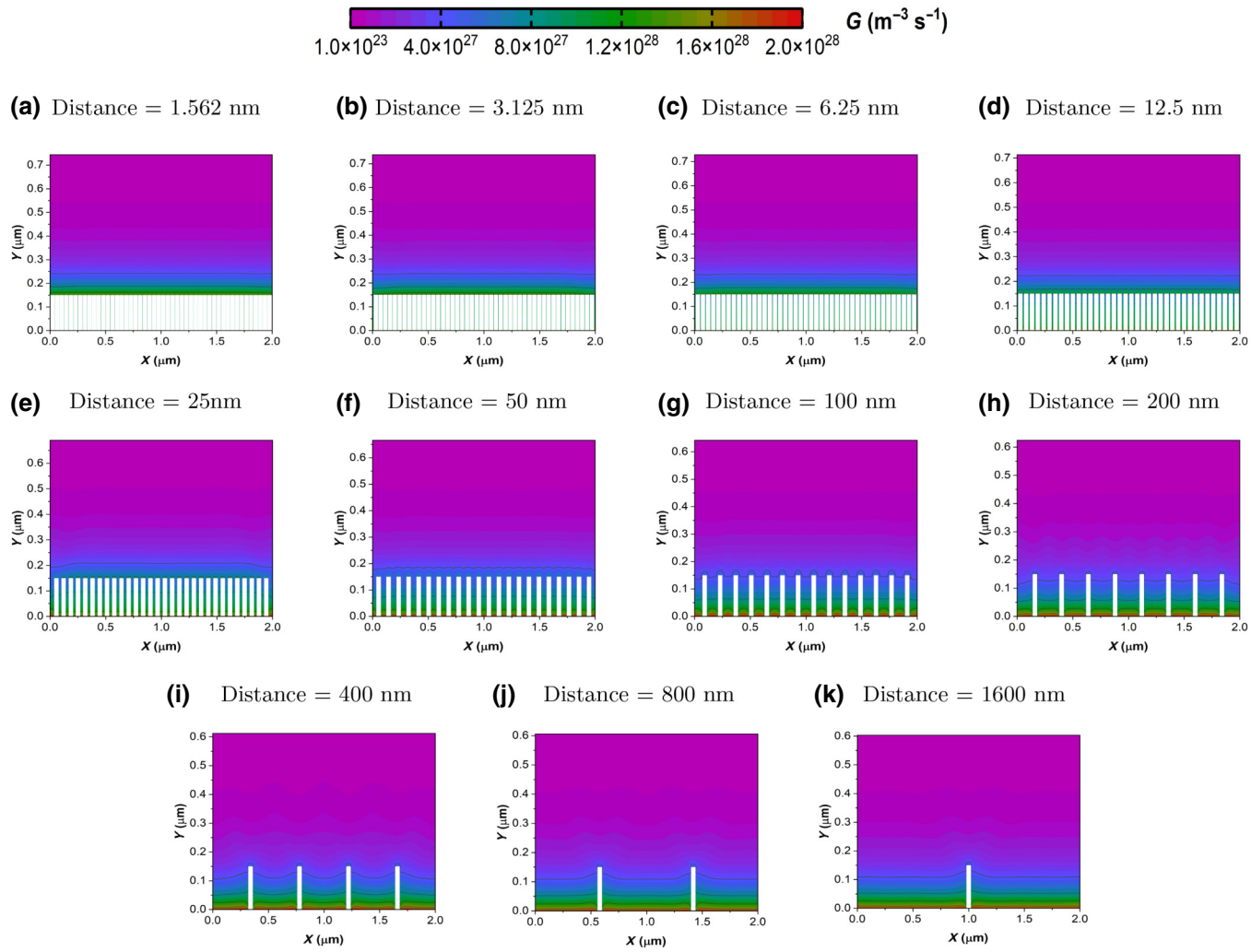

FIG. 9. Perovskite-layer 2D spatial charge-generation profile maps for PSCs with structured ETLs with different density of SnO_2 nanorods. Distance: (a) 1.562 nm, (b) 3.125 nm, (c) 6.25 nm, (d) 12.5 nm, (e) 25 nm, (f) 50 nm, (g) 100 nm, (h) 200 nm, (i) 400 nm, (j) 800 nm, and (k) 1600 nm.

2D spatial charge-carrier generation-rate profile maps of structured PSCs with different internanorod densities under 1-Sun condition are presented in Fig. 9.

Figure 10 shows the estimated values for the photovoltaic parameters of structured devices as functions of the internanorod distance (D). Figure 10(a) indicates that J_{SC} of devices increases and approaches its saturation value as D increases and reaches its maximum value at 1600 nm. The J_{SC} saturation value obtained here is similar to that of reference planar devices. Figure 10(b) shows that V_{OC} of structured devices slightly increases as D becomes larger. However, at around $D = 100$ nm, V_{OC} decreases again, eventually stabilizing at a V_{OC} value that is similar to the one obtained for reference planar devices. Variation of D appears to have very little effect on FF of structured devices as shown in Fig. 10(c). For the entire range of D, FF remains almost constant. The dependence of device performance on D [Fig. 10(d)] shows that with the increase in the internanorod distance, PCE of devices also gets boosted and reaches its saturation value at large distances. This is due to a relatively large variation of device J_{SC} with D, which strongly impacts the overall device performance. As in J_{SC} and V_{OC}, the saturation value for PCE of structured devices also coincides with the PCE of reference planar devices at large D values. These findings indicate that fewer SnO_2 nanorods or the complete absence of them in the structure of ETLs, improve the performance of PSCs.

E. Performance of reference planar and structured PSCs versus charge-carrier diffusion length

So far, comparison of the device behavior for reference planar and structured devices is conducted by considering optimal conditions in terms of electronic properties for the perovskite layer. In reality, however, the perovskite layer

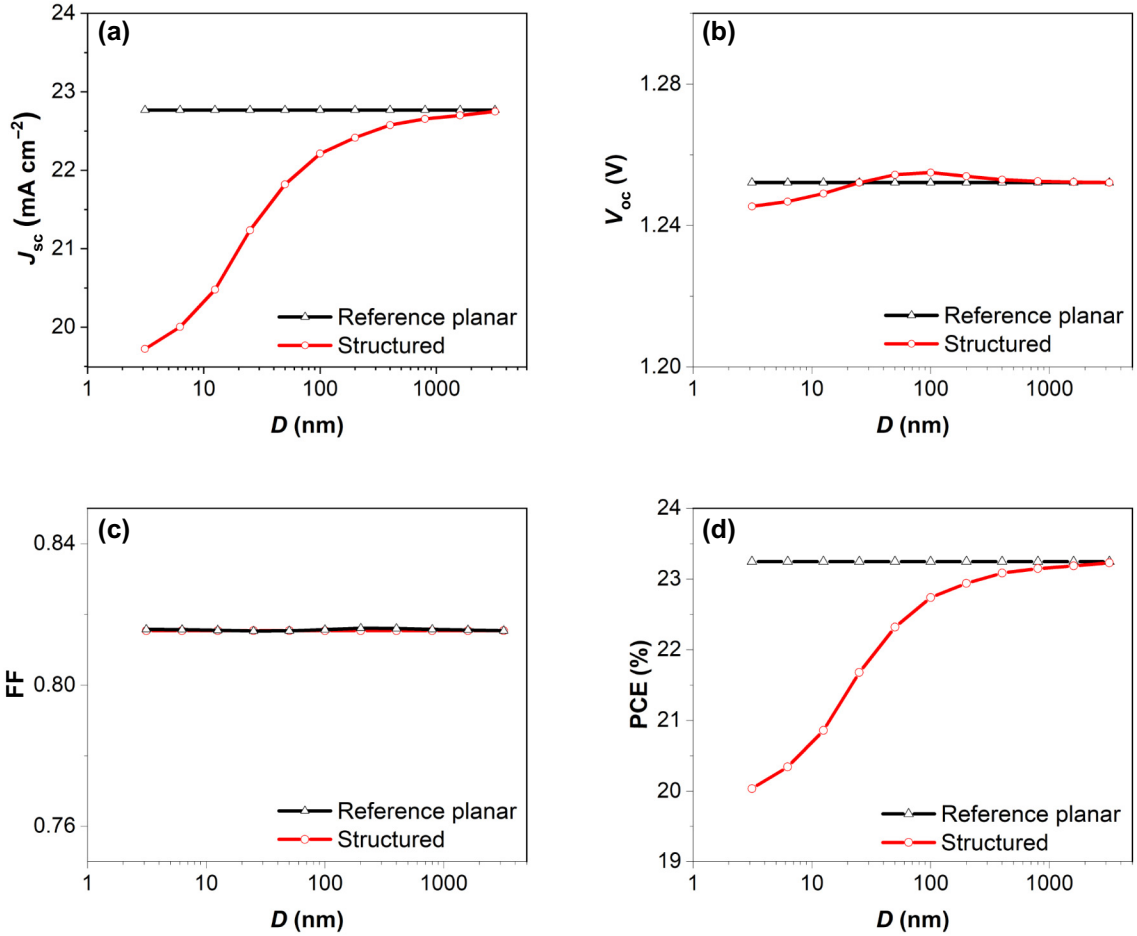

FIG. 10. Dependences of (a) J_{SC}, (b) V_{OC}, (c) FF, and (d) PCE of structured PSCs on D (internanorod distance) of ETL SnO_2 nanorods.

in PSCs does not always have the ideal physical properties. The polycrystalline nature, as well as the presence of many bulk and surface defects, changes the electronic properties of experimentally obtained perovskite films used in PSCs. One of the useful electronic parameters that characterizes these aspects of the perovskite-layer quality is charge-carrier diffusion length $L_{n,p}$ in the material. Thus, it is also useful to examine how the behavior of reference planar and structured ($h = 150$ nm and $w = 40$ nm) PSCs is affected by this parameter.

Figure 11 shows the dependence of the device photovoltaic parameters on $L_{n,p}$. Here, the $L_{n,p}$ is varied by keeping the electron and hole mobility values constant ($\mu_{n,p} = 0.1$ cm^2 V^{-1} s^{-1}) and varying the electron and hole lifetimes ($\tau_{n,p}$) from 3.9 ns to 1024 μs. Figure 11(a) shows that J_{SC} in both devices increase with $L_{n,p}$ and reach its saturation values at large $L_{n,p}$. The J_{SC} value of reference planar devices is higher than that of structured devices at large $L_{n,p}$, which is consistent with the results presented above (see Fig. 6). However, for smaller $L_{n,p}$ (around $L_{n,p} = 60$ nm), the J_{SC} curve for reference planar devices crosses the one for structured devices, which, in turn, becomes higher than J_{SC} of reference planar devices at $L_{n,p}$ values smaller than 60 nm. The V_{OC} values in both cases also increase with $L_{n,p}$ and exhibit similar trends except for a small deviation at very small $L_{n,p}$ values [see Fig. 11(b)]. Figure 11(c) shows that FF for both devices are increasing functions of $L_{n,p}$ and saturates at values around 0.8. However, at smaller $L_{n,p}$ values (< 2 μm), FF of structured devices becomes higher than that of reference planar devices; this becomes even more pronounced at smaller $L_{n,p}$ values.

Due to the aforementioned trends in the behavior of J_{SC}, V_{OC}, and FF with respect to the perovskite layer $L_{n,p}$, PCEs of reference planar and structured devices also experience an increase and subsequent saturation with the increase in $L_{n,p}$, as shown in Fig. 11(d). However, because of the crossing of J_{SC} curves for reference planar and structured devices as well as higher FF values for structured devices at lower $L_{n,p}$, the respective PCE curves also exhibit crossing at $L_{n,p} = 0.5$ μm. Below this value, PCE of structured devices is slightly higher than that of reference planar ones.

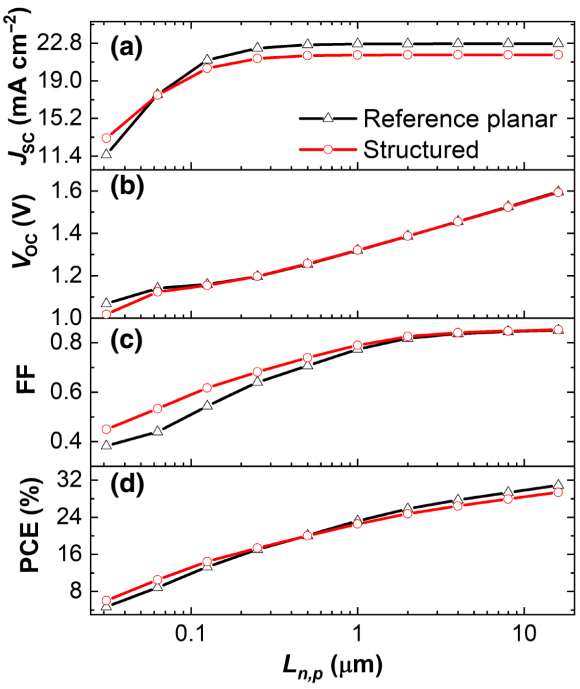

FIG. 11. Dependence of (a) J_{SC}, (b) V_{OC}, (c) FF, and (d) PCE of reference planar and structured PSCs on $L_{n,p}$ (charge-carrier diffusion length) of the perovskite layer.

Above this value, the situation reverses and PCE of reference planar devices become slightly higher than that of their structured counterparts.

F. Charge-carrier recombination in reference planar and structured PSCs

The observed crossing of the PCE versus $L_{n,p}$ curves [see Fig. 11(d)] in reference planar and structured devices can be better explained by analyzing the recombination processes in these devices. Figure 11(d) depicts that at $L_{n,p} = 0.031$ μm, the PCE of reference planar devices (4.71%) is smaller than the PCE of structured devices (6.05%) by almost 30%, whereas at $L_{n,p} = 2$ μm, the PCE of reference planar devices (25.82%) is higher than the PCE of structured device (24.77%) by around 4%. The main contributor to the PCEs of devices at these $L_{n,p}$ values is the J_{SC} values [see Fig. 11(a)]. Approximately, the difference in the J_{SC} values of reference planar and structured devices at $L_{n,p} = 0.031$ and 2 μm can be rationalized by the difference of average carrier generation (G_{avg}) and recombination (R_{avg}) in devices at short-circuit condition [see Eqs. (14) and (15)]. Figure 12 shows the calculated 2D spatial charge-carrier recombination-rate profile maps of the perovskite layer in reference planar and structured devices at $L_{n,p} = 0.031$ and 2 μm. These carrier-recombination rate profile maps are used to estimate the R_{avg} values in devices as it is done for G_{avg} above. Table IV shows the G_{avg} and R_{avg} values for reference planar and structured devices at $L_{n,p} = 0.031$ and 2 μm, respectively, and also their difference ($\Delta = G_{avg} - R_{avg}$) for the same $L_{n,p}$ values. The Δ value of reference planar devices is smaller than that of structured devices at $L_{n,p}$ = 0.031 μm, whereas at $L_{n,p} = 2$ μm, Δ of structured devices is smaller than the corresponding one of reference devices. This result is consistent with the trends in J_{SC} of reference planar and structured devices at $L_{n,p} = 0.031$ and 2 μm values and gives a certain insight into the cause of PCE crossing at moderate $L_{n,p}$ values [see Figs. 11(a) and 11(d)].

The aforementioned findings indicate that ETL SnO_2 nanorods in structured devices can be useful in extracting photogenerated charge carriers from the perovskite at small $L_{n,p}$ values (e.g., $L_{n,p} = 0.031$ μm). This might be due to the interpenetrating nature of the ETL and perovskite layers, which can help to collect photogenerated electrons deeper within the volume of the perovskite layer [see Fig. 13(a)]. However, at $L_{n,p}$ values that are comparable or larger than the thickness of the perovskite layer (e.g., $L_{n,p} = 2$ μm), a more homogeneously distributed electric field in the perovskite layer of reference planar PSCs (see Fig. 7) helps to drive photogenerated charge carriers towards their respective contacts more effectively. Due to this feature, a better charge extraction is enabled in reference planar devices as compared to structured PSCs [see Fig. 13(b)].

An interesting aspect of the crossing of the PCEs of reference planar and structured devices, which takes place at $L_{n,p}$ values around 0.5 μm [see Fig. 11(d)], is the value of PCE (approximately 20%) at the crossing point. It is noteworthy that in the literature, most of the experimentally obtained structured devices with various 1D metal-oxide ETLs usually have PCE values below 20% [10–30,52–54]. This is especially true for those works that report improved performance in structured devices as compared to their reference planar alternatives [11,23,24]. Some of the notable examples of the reports by other groups, in which comparison of the performance of reference planar and structured devices either with simple (e.g., $MAPbI_3$) or more complex (e.g., $Cs_{(1-x1-x2)}FA_{x1}MA_{x2}Pb(I_{(1-y)}Br_y)_3$) perovskites are carried out, are listed in Table V. Here, the examples are shown for SnO_2, TiO_2, and ZnO ETLs and the type of devices is indicated as "RP" (for reference planar) and "NR" (for nanorod) in the brackets next to their ETLs. Contrasting the theoretical findings in this work with the experimental findings reported in the literature suggest that the $L_{n,p}$ in these devices are possibly below or close to 0.5 μm. As mentioned above, the state-of-the-art high-performing PSCs are planar devices with large perovskite crystallites and long carrier-diffusion lengths [31–34]. Even PSCs with $MAPbI_3$ can produce PCEs above 21% if the perovskite layer is made of a rather thick single crystal, as reported by Chen *et al.* [55]. Considering these, it is, perhaps, the case that structured

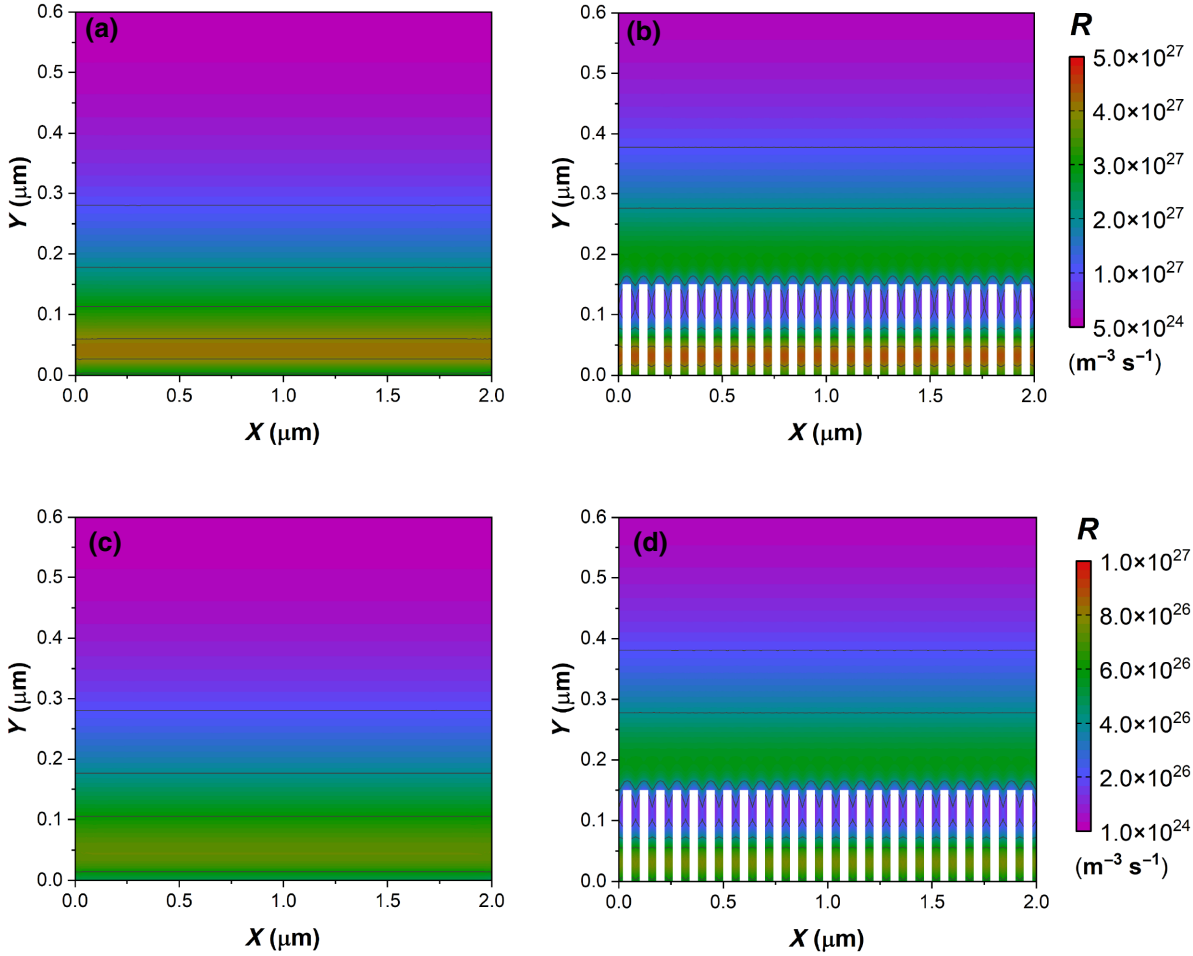

FIG. 12. Perovskite-layer 2D spatial charge-carrier recombination profile maps for reference planar and structured devices at $L_{n,p} = 0.031$ μm (a),(b) and $L_{n,p} = 2$ μm (c),(d). The height and width of SnO_2 nanorods are 150 and 40 nm, respectively.

devices will not outperform their reference planar counterparts that are made in the same way and employ the same type of ETLs with the same chemical composition. An experimental validation of this will require a careful control over charge-carrier diffusion length in the perovskite layer of reference planar and structured devices and the uniformity of the density as well as the aspect ratio of ETL metal-oxide nanorods in structured devices.

Overall, the findings of this work indicate that structuring of SnO_2 ETLs of PSCs as 1D arrays of nanorods can help to increase the overall light-harvesting ability of resulting devices. However, reference planar devices appear to deliver higher performance than structured counterparts for conditions when the physical properties of the functional layer materials in both devices are optimal and have the same parameters. This trend, however, reverses when the perovskite layers of devices have less ideal physical properties such as short charge-carrier diffusion lengths. In the light of these observations, it is possible to suggest that the difficulty in obtaining state-of-the-art PCEs for PSCs with structured ETLs could be associated with the physical limitations (e.g., inhomogeneous electric

TABLE IV. Average generation (G_{avg}) and recombination (R_{avg}) rates for reference planar and structured devices, and $\Delta = G_{avg} - R_{avg}$ at $L_{n,p} = 0.031$ and 2 μm.

	$L_{n,p} = 0.031\ \mu m$		$L_{n,p} = 2\ \mu m$	
	Reference planar	Structured	Reference planar	Structured
$G_{avg}\ (m^{-3}s^{-1})$	2.62×10^{27}	2.90×10^{27}	2.62×10^{27}	2.90×10^{27}
$R_{avg}\ (m^{-3}s^{-1})$	1.29×10^{27}	0.69×10^{27}	0.11×10^{27}	0.42×10^{27}
$\Delta = G_{avg} - R_{avg}\ (m^{-3}s^{-1})$	1.33×10^{27}	2.21×10^{27}	2.51×10^{27}	2.48×10^{27}

TABLE V. Comparison of the PCEs of experimental reference planar and structured devices reported in the literature and fabricated the same way.

No.	Front electrode/ETL/perovskite/HTL/back electrode	PCE(%)	Ref.
1	FTO/SnO_2 (RP) /$(FAPbI_3)_{0.85}(MAPbBr_3)_{0.15}$/SpiroOMeTAD/Au	11.54 ± 0.84	[40]
	FTO/SnO_2 (NR) /$(FAPbI_3)_{0.85}(MAPbBr_3)_{0.15}$/SpiroOMeTAD/Au	14.90 ± 0.56	
2	FTO/SnO_2(RP)/$MAPbI_3$/SpiroOMeTAD/AgAl	12.04 ± 1.08	[11]
	FTO/SnO_2(NR)/$MAPbI_3$/SpiroOMeTAD/AgAl	16.57 ± 1.09	
3	FTO/SnO_2(RP)/$Cs_{(1-x1-x2)}FA_{x1}MA_{x2}Pb(I_{(1-y)}Br_y)_3$/SpiroOMeTAD/Au	18.95 ± 0.58	[53]
	FTO/SnO_2(NR)/$Cs_{(1-x1-x2)}FA_{x1}MA_{x2}Pb(I_{(1-y)}Br_y)_3$/SpiroOMeTAD/Au	19.25 ± 0.40	
4	FTO/TiO_2(RP)/$Cs_{0.05}(FA_{0.83}MA_{0.17})_{0.95}Pb(I_{0.83}Br_{0.17})_3$/SpiroOMeTAD/Au	14.96 ± 0.28	[20]
	FTO/TiO_2(NR)/$Cs_{0.05}(FA_{0.83}MA_{0.17})_{0.95}Pb(I_{0.83}Br_{0.17})_3$/SpiroOMeTAD/Au	15.97 ± 0.33	
5	FTO/TiO_2(RP)/$MAPbI_3$/SpiroOMeTAD/Au	11.61 ± 0.60	[23]
	FTO/TiO_2(NR)/$MAPbI_3$/SpiroOMeTAD/Au	14.02 ± 0.50	
6	FTO/TiO_2(RP)/$MAPbI_{3-x}Br_x$/SpiroOMeTAD/Au	10.54 ± 2.28	[52]
	FTO/TiO_2(NR)/$MAPbI_{3-x}Br_x$/SpiroOMeTAD/Au	13.41 ± 2.52	
7	FTO/ZnO(RP)/$MAPbI_3$/SpiroOMeTAD/Ag	11.10 ± 0.05	[24]
	FTO/ZnO(NR)/$MAPbI_3$/SpiroOMeTAD/Ag	14.23 ± 0.01	

field distribution within the perovskite layer and increased carrier recombination losses) that are inherent to the design of structured devices. Nevertheless, it should be noted that the findings presented here are only the estimates of the real-life device properties. The assumptions made in constructing the theoretical models of devices are rather coarse and the computational methods employed here are unable to accommodate the actual nature of structured ETLs and experimental processing conditions. Particularly, the simulation of real physical processes taking place at the interfaces between the device functional layers are challenging within the framework of the computational methods used here; especially the ETL-perovskite interface, which is the principal interface that distinguishes planar and structured devices. Hence, detailed research is still required further to make more conclusive statements on the comparative performance of planar and structured PSCs.

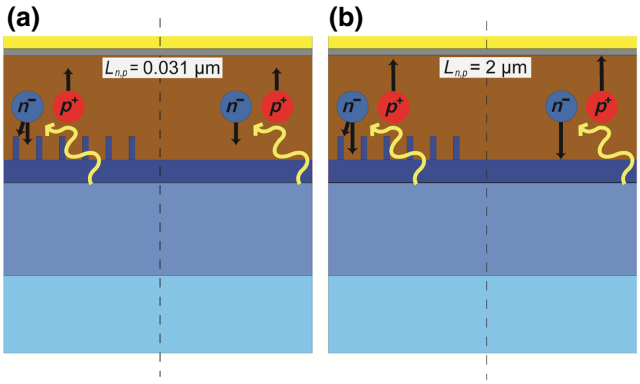

FIG. 13. Schematic representation of charge-carrier collection in structured and reference planar devices at (a) $L_{n,p} = 0.031$ and (b) $L_{n,p} = 2$ μm.

IV. CONCLUSIONS

In conclusion, numerical simulation methods are employed to examine the performance of PSCs with SnO_2 nanorod-based ETLs and contrasted with the performance of PSCs with simple planar SnO_2 ETLs. The aspect ratio of SnO_2 nanorods and their density are varied to examine their influence on the light-harvesting ability and the photovoltaic parameters of devices. Employing SnO_2 nanorod-based ETLs in constructing devices can increase the overall light-harvesting ability of the corresponding devices. However, it is found that the performance of reference planar devices always remains higher than the one of the structured counterparts, irrespective of the aspect ratio and the density of ETL SnO_2 nanorods. The structured devices exhibit a higher PCE only under the condition when the charge-carrier diffusion length is shorter than 0.5 μm. The analysis of the electric field, current density, and carrier-recombination distributions within the body of devices reveals that the use of structured ETLs lead to less favorable conditions for charge-carrier separation as compared to devices with reference planar ETLs. Overall, the results presented in this work unveil some of the fundamental differences in the device physics and the working principles of planar and structured PSCs with SnO_2 ETLs. The findings of this study can be used as a guide for designing and studying experimental PSCs with a variety of different ETLs.

ACKNOWLEDGMENTS

This work is supported by Scientific Research Grants from Ministry of Education and Science of the Republic of Kazakhstan (Grants No. AP14869871, No. AP08052412, and No. AP14869983), Nazarbayev University Faculty Development Competitive Research Grant (Grant No.

110119FD4512), and Nazarbayev University Collaborative Research Grant (Grant No. 021220CRP1922).

A.N.J. thanks Scientific Research Grants from Ministry of Education and Science of the Republic of Kazakhstan (Grants No. AP14869871 and No. AP08052412), Nazarbayev University Faculty Development Competitive Research Grant (Grant No. 110119FD4512), and Nazarbayev University Collaborative Research Grant (Grant No. 021220CRP1922). A.N. thanks the grant from Ministry of Education and Science of the Republic of Kazakhstan (Grant No. AP14869983).

Assylan Akhanuly: data curation, formal analysis, investigation, visualization, validation, and writing—original draft. Iliyas T. Dossyaev: data curation, formal analysis, investigation, visualization, validation, and writing—original draft. Erik O. Shalenov: formal analysis, investigation, methodology, validation, and writing—original draft. Constantinos Valagiannopoulos: data curation, formal analysis, investigation, methodology, and validation. Karlygash N. Dzhumagulova: methodology. Annie Ng: conceptualization, methodology, and funding acquisition. Askhat N. Jumabekov: conceptualization, formal analysis, funding acquisition, project administration, resources, supervision, and writing—review and editing.

The authors declare that they have no competing financial interests or personal relationships that could have appeared to influence the work reported in this paper.

DATA AVAILABILITY

The data supporting the findings of this study are available from the corresponding author upon reasonable request.

[1] S. Bellani, A. Bartolotta, A. Agresti, G. Calogero, G. Grancini, A. Di Carlo, E. Kymakis, and F. Bonaccorso, Solution-processed two-dimensional materials for next-generation photovoltaics, Chem. Soc. Rev. **50**, 11870 (2021).

[2] M. Mangrulkar and K. J. Stevenson, The progress of additive engineering for $CH_3NH_3PBI_3$ photo-active layer in the context of perovskite solar cells, Crystals **11**, 814 (2021).

[3] J. Li, Z. Han, Y. Gu, D. Yu, J. Liu, D. Hu, X. Xu, and H. Zeng, Perovskite single crystals: Synthesis, optoelectronic properties, and application, Adv. Funct. Mater. **31**, 2008684 (2021).

[4] M. Lyu, J. H. Yun, P. Chen, M. Hao, and L. Wang, Addressing toxicity of lead: Progress and applications of low-toxic metal halide perovskites and their derivatives, Adv. Energy Mater. **7**, 1602512 (2017).

[5] Z. Yelzhanova, G. Nigmetova, D. Aidarkhanov, B. Daniyar, B. Baptayev, M. P. Balanay, A. N. Jumabekov, and A. Ng, A morphological study of solvothermally grown SnO_2 nanostructures for application in perovskite solar cells, Nanomaterials **12**, 1686 (2022).

[6] Best research-cell efficiency chart, https://www.nrel.gov/pv/cell-efficiency.html [NREL, accessed September 4, 2022].

[7] A. Kojima, K. Teshima, Y. Shirai, and T. Miyasaka, Organometal halide perovskites as visible-light sensitizers for photovoltaic cells, J. Am. Chem. Soc. **131**, 6050 (2009).

[8] N. Ali, N. Shehzad, S. Uddin, R. Ahmed, M. Jabeen, A. Kalam, A. G Al-Sehemi, H. Alrobei, M. B Kanoun, and A. Khesro, *et al.*, A review on perovskite materials with solar cell prospective, Int. J. Energy Res. **45**, 19729 (2021).

[9] Y. Chen, Q. Meng, L. Zhang, C. Han, H. Gao, Y. Zhang, and H. Yan, SnO_2-based electron transporting layer materials for perovskite solar cells: A review of recent progress, J. Energy Chem. **35**, 144 (2019).

[10] X. Zhang, Y. Rui, Y. Wang, J. Xu, H. Wang, Q. Zhang, and P. Müller-Buschbaum, SnO_2 nanorod arrays with tailored area density as efficient electron transport layers for perovskite solar cells, J. Power Sources **402**, 460 (2018).

[11] C. Zhang, X. Deng, J. Zheng, X. Zhou, J. Shi, X. Chen, Z. Sun, and S. Huang, Solution-synthesized SnO_2 nanorod arrays for highly stable and efficient perovskite solar cells, Electrochim. Acta. **283**, 1134 (2018).

[12] Q. Liu, M.-C. Qin, W.-J. Ke, X.-L. Zheng, Z. Chen, P.-L. Qin, L.-B. Xiong, H.-W. Lei, J.-W. Wan, and J. Wen, *et al.*, Enhanced stability of perovskite solar cells with low-temperature hydrothermally grown SnO_2 electron transport layers, Adv. Funct. Mater. **26**, 6069 (2016).

[13] G. Yang, H. Lei, H. Tao, X. Zheng, J. Ma, Q. Liu, W. Ke, Z. Chen, L. Xiong, and P. Qin, *et al.*, Reducing hysteresis and enhancing performance of perovskite solar cells using low-temperature processed Y-doped SnO_2 nanosheets as electron selective layers, Small **13**, 1601769 (2016).

[14] C. Gao, S. Yuan, B. Cao, and J. Yu, SnO_2 nanotube arrays grown via an in situ template-etching strategy for effective and stable perovskite solar cells, Chem. Eng. J. **325**, 378 (2017).

[15] X. Zhang, Y. Rui, J. Yang, L. Wang, Y. Wang, and J. Xu, Monodispersed SnO_2 microspheres aggregated by tunable building units as effective photoelectrodes in solar cells, Appl. Surf. Sci. **463**, 679 (2019).

[16] X. Fan, Y. Rui, X. Han, J. Yang, Y. Wang, and Q. Zhang, Spray-coated monodispersed SnO_2 microsphere films as scaffold layers for efficient mesoscopic perovskite solar cells, J. Power Sources **448**, 227405 (2020).

[17] C. Liu, R. Zhu, A. Ng, Z. Ren, S. H. Cheung, L. Du, S. K. So, J. A. Zapien, A. B. Djurišić, and D. L. Phillips, *et al.*, Investigation of high performance TiO_2 nanorod array perovskite solar cells, J. Mater. Chem. A **5**, 15970 (2017).

[18] U. K. Thakur, A. M. Askar, R. Kisslinger, B. D. Wiltshire, P. Kar, and K. Shankar, Halide perovskite solar cells using monocrystalline TiO_2 nanorod arrays as electron transport layers: Impact of nanorod morphology, Nanotechnology **28**, 274001 (2017).

[19] F. Yu, G. S. Han, Y. J. Tu, H.-S. Roh, and J.-K. Lee, Electron extraction mechanism in low hysteresis perovskite solar cells using single crystal TiO_2 nanorods, Sol. Energy **167**, 251 (2018).

[20] Z. Hu, J. M. García-Martín, Y. Li, L. Billot, B. Sun, F. Fresno, A. García-Martín, M. U. González, L. Aigouy, and

Z. Chen, TiO_2 nanocolumn arrays for more efficient and stable perovskite solar cells, ACS Appl. Mater. Interfaces **12**, 5979 (2020).

[21] Y. Lv, R. Yuan, B. Cai, B. Bahrami, A. H. Chowdhury, C. Yang, Y. Wu, Q. Qiao, S. Liu, and W.-H. Zhang, High-efficiency perovskite solar cells enabled by anatase TiO_2 nanopyramid arrays with an oriented electric field, Angew. Chem. Int. **59**, 11969 (2020).

[22] J. Peng, D. Walter, Y. Ren, M. Tebyetekerwa, Y. Wu, T. Duong, Q. Lin, J. Li, T. Lu, and M. A. Mahmud, *et al.*, Nanoscale localized contacts for high fill factors in polymer-passivated perovskite solar cells, Science **371**, 390 (2021).

[23] W.-Q. Wu, F. Huang, D. Chen, Y.-B. Cheng, and R. Caruso, Solvent-mediated dimension tuning of semiconducting oxide nanostructures as efficient charge extraction thin films for perovskite solar cells with efficiency exceeding 16%, Adv. Energy Mater. **6**, 1502027 (2016).

[24] S. Yun, T. Guo, Y. Li, X. Gao, A. Huang, and L. Kang, Well-ordered vertically aligned ZnO nanorods arrays for high-performance perovskite solar cells, Mater. Res. Bull. **130**, 110935 (2020).

[25] M. H. Kumar, N. Yantara, S. Dharani, M. Graetzel, S. Mhaisalkar, P. P. Boix, and N. Mathews, Flexible, low-temperature, solution processed ZnO-based perovskite solid state solar cells, Chem. Commun. **49**, 11089 (2013).

[26] N. Islavath, D. Das, S. V. Joshi, and E. Ramasamy, Seed layer-assisted low temperature solution growth of 3D ZnO nanowall architecture for hybrid solar cells, Mater. Des. **116**, 219 (2017).

[27] J.-F. Tang, Z.-L. Tseng, L.-C. Chen, and S.-Y. Chu, ZnO nanowalls grown at low-temperature for electron collection in high-efficiency perovskite solar cells, Sol. Energy Mater. Sol. Cells **154**, 18 (2016).

[28] J. Zhang, P. Barboux, and T. Pauporté, Electrochemical design of nanostructured ZnO charge carrier layers for efficient solid-state perovskite-sensitized solar cells, Adv. Energy Mater. **4**, 1400932 (2014).

[29] K. Mahmood, A. Khalid, and M. T. Mehran, Nanostructured ZnO electron transporting materials for hysteresis-free perovskite solar cells, Sol. Energy **173**, 496503 (2018).

[30] C. M. Pelicano and H. Yanagi, Efficient solid-state perovskite solar cells based on nanostructured zinc oxide designed by strategic low temperature water oxidation, J. Mater. Chem. C **5**, 8059 (2017).

[31] J. J. Yoo, G. Seo, M. R. Chua, T. G. Park, Y. Lu, F. Rotermund, Y.-K. Kim, C. S. Moon, N. J. Jeon, and J.-P. Correa-Baena, *et al.*, Efficient perovskite solar cells via improved carrier management, Nature **590**, 587 (2021).

[32] Q. Jiang, Z. Chu, P. Wang, X. Yang, H. Liu, Y. Wang, Z. Yin, J. Wu, X. Zhang, and J. You, Planar-structure perovskite solar cells with efficiency beyond 21%, Adv. Mater. **29**, 1703852 (2017).

[33] E. H. Jung, N. J. Jeon, E. Y. Park, C. S. Moon, T. J. Shin, T.-Y. Yang, J. H. Noh, and J. Seo, Efficient, stable and scalable perovskite solar cells using poly(3-hexylthiophene), Nature **567**, 511 (2019).

[34] Q. Jiang, Y. Zhao, X. Zhang, X. Yang, Y. Chen, Z. Chu, Q. Ye, X. Li, Z. Yin, and J. You, Surface passivation of perovskite film for efficient solar cells, Nat. Photon. **13**, 460 (2019).

[35] J. Burschka, N. Pellet, S.-J. Moon, R. Humphry-Baker, P. Gao, M. K. Nazeeruddin, and M. Grätze, Sequential deposition as a route to high-performance perovskite-sensitized solar cells, Nature **499**, 316 (2013).

[36] W. S. Yang, J. H. Noh, N. J. Jeon, Y. C. Kim, S. Ryu, J. Seo, and S.-I Seok, High-performance photovoltaic perovskite layers fabricated through intramolecular exchange, Science **348**, 1234 (2015).

[37] W. S. Yang, B. W.. Park, E. H. Jung, N. J. Jeon, Y. C. Kim, D. U. Lee, S. S. Shin, J. Seo, E. K. Kim, and J. H. Noh, *et al.*, Iodide management in formamidinium-lead-halide–based perovskite layers for efficient solar cells, Science **356**, 1376 (2017).

[38] E. O. Shalenov, K. N. Dzhumagulova, A. Ng, and A. N. Jumabekov, Performance optimization of back-contact perovskite solar cells with quasi-interdigitated electrodes, Sol. Energy **205**, 102 (2020).

[39] E. O. Shalenov, K. N. Dzhumagulova, Y. S. Seitkozhanov, A. Ng, C. Valagiannopoulos, and A. N. Jumabekov, Insights on desired fabrication factors from modeling sandwich and quasi-interdigitated back-contact perovskite solar cells, ACS Appl. Energy Mater. **4**, 1093 (2021).

[40] E. O. Shalenov, Y. S. Seitkozhanov, C. Valagiannopoulos, A. Ng, K. N. Dzhumagulova, and A. N. Jumabekov, Performance evaluation of different designs of back-contact perovskite solar cells, Sol. Energy Mater. Sol. Cells **234**, 111426 (2022).

[41] X. Li, N. P. Hylton, V. Giannini, K. H. Lee, N. J. Ekins-Daukes, and S. A. Maier, Multi-dimensional modeling of solar cells with electromagnetic and carrier transport calculations, Prog. Photovoltaics Res. Appl. **21**, 109 (2013).

[42] H. P. Parkhomenko, E. O. Shalenov, Z. Umatova, K. N. Dzhumagulova, and A. N. Jumabekov, Fabrication of flexible quasi-interdigitated back-contact perovskite solar cells, Energies **15**, 3056 (2022).

[43] S. M. Sze and K. K. Ng, *Physics of Semiconductor Devices* (Wiley-Interscience, Hoboken, 2006), 832

[44] Z. Yang, W. Yang, X. Yang, J. C. Greer, J. Sheng, B. Yan, and J. Ye, Device physics of back-contact perovskite solar cells, Energy Environ. Sci. **13**, 1753 (2020).

[45] W. Shockley and W. T. Read, Statistics of the recombinations of holes and electrons, Phys. Rev. **87**, 835 (1952).

[46] See Supplemental Material at http://link.aps.org/supplemental/10.1103/PhysRevApplied.19.054039 for details on the methods and discussion of parameters.

[47] T. A. König, P. A. Ledin, J. Kerszulis, M. A. Mahmoud, M. A. El-Sayed, J. R. Reynolds, and V. V. Tsukruk, Electrically tunable plasmonic behavior of nanocube–polymer nanomaterials induced by a redox-active electrochromic polymer, ACS Nano **8**, 6182 (2014).

[48] M. Filipič, P. Löper, B. Niesen, S. De Wolf, J. Krč, C. Ballif, and M. Topič, $CH_3NH_3PbI_3$ perovskite/silicon tandem solar cells: characterization based optical simulations, Opt. Express **23**, A263 (2015).

[49] M. Rubin, Optical properties of soda lime silica glasses, Sol. Energy Mater. **12**, 275 (1985).

[50] K. M. McPeak, S. V. Jayanti, S. J. Kress, S. Meyer, S. Iotti, A. Rossinelli, and D. J. Norris, Plasmonic films can easily be better: Rules and Recipes, ACS Photonics **2**, 326 (2015).

[51] G. A. Casas, M. A. Cappelletti, A. P. Cédola, B. M. Soucase, and E. L. Peltzer y Blancá, Analysis of the power conversion efficiency of perovskite solar cells with different materials as hole-transport layer by numerical simulations, Superlattices Microstruct. **107**, 136 (2017).

[52] G. Xiao, C. Shi, Z. Zhang, N. Li, and L. Li, Short-length and high-density TiO_2 nanorod arrays for the efficient charge separation interface in perovskite solar cells, J. Solid State Chem. **249**, 169 (2017).

[53] Y. Xu, Y. Rui, X. Wang, B. Li, Z. Jin, Y. Wang, and Q. Zhang, Boosted charge extraction of SnO_2 nanorod arrays via nanostructural and surface chemical engineering for efficient and stable perovskite solar cells, Appl. Surface Sci. **607**, 154986 (2023).

[54] X. Li, S.-M. Dai, P. Zhu, L.-L. Deng, S.-Y. Xie, Q. Cui, H. Chen, N. Wang, and H. Lin, Efficient perovskite solar cells depending on TiO_2 nanorod arrays, ACS Appl. Mater. Interfaces **8**, 21358 (2016).

[55] Z. Chen, B. Turedi, A. Y. Alsalloum, C. Yang, X. Zheng, I. Gereige, A. AlSaggaf, O. F. Mohammed, and O. M. Bakr, Single-crystal $MAPbI_3$ perovskite solar cells exceeding 21% power conversion efficiency, ACS Energy Lett. **4**, 1258 (2019).